ISSN 0354-8724 (hard copy) | ISSN 1820-7138 (online)

Using Geostatistics to Generate a Geological Model of a Sandstone Petroleum Reservoir in Southern California

Diego A. Vasquez[A*], **Jennifer Swift**[A]

Received: July 21, 2021 | Revised: December 17, 2021 | Accepted: December 21, 2021
doi: 10.5937/gp26-33244

Abstract

A variogram-based two-point geostatistical approach was applied to generate a geological model of a petroleum reservoir. The geology consists of a sandstone formation with uniformly inclined rock strata of equal dip angle structurally trapped by surrounding faults. Data exploration of electrical well logs using univariate/bivariate statistical tests and data transformation tools demonstrated the data to be statistically suitable for ordinary kriging and sequential Gaussian simulation. Three directions were defined as part of the variogram and the data were interpolated resulting in a 3D subsurface representation. Validation included performing a leave-one-out cross-validation for each well and statistical comparison of multiple realizations generated from a computed stochastic model. The results display a reliable geological model which indicate a direct causation of the continuity trends from the bedding attitude of the regional fault trap.

Keywords: Reservoir Characterization; Ordinary Kriging; Conditional Simulation; Geostatistics; GIS; Petroleum Geology; Los Angeles Basin

Introduction

Reservoir characterization includes estimating the distribution of subsurface properties of a geologic system, which is essential for improving resource management, production development and field operations (Gorell, 1995). Reliable geologic outputs obtained from geostatistical models are used in a variety of important practices such as calculating production rates, remediating contaminated aquifers, estimating the recoverable reserves (i.e., oil, gas or water), drilling new boreholes and determining hydrocarbon migration (Deutsch, 2006). An important question for reservoir characterization is to determine the extent of geological continuity. This report demonstrates how to generate a geological model using two-point geostastistics and thereby revealing the geological continuity.

Interpolation of subsurface data involves predicting values of specific variables at unsampled locations based on the measurements obtained from known locations using statistical principles, thereby creating a continuous surface of the geologic domain (Journel, 2000) (Dubrule & Damsleth, 2001). The inclusion of geological features depends mainly on the depositional environment and defines the overall geological architecture of a given reservoir (Ebong et al., 2021). Different geological settings may require different geostatistical approaches in order to construct an appropriate model that honors the character of the reservoir with the greatest possible accuracy (Ebong et al., 2021; Caumon, 2010). The assumption of stationarity is important in geostatistics, and it is defined in practice as local

---

[A] Spatial Sciences Institute, University of Southern California, 3551 Trousdale Parkway, Los Angeles, California 90089 United States
[*] Corresponding author: Diego Vasquez, e-mail: diego.vasquez@usc.edu

data averages within a spatial domain that are approximately constant (Elfadil et al., 2018). Assuming stationarity for a particular area requires that the model developed from the sampled data be applicable within the specified area of stationarity (Kelkar & Perez, 2002). In the context of this investigation, the area of stationarity defined by the continuity boundaries for the subsurface field is the reservoir. In reservoir analyses this assumption is necessarily subjective because of the inherent uncertainties in the subsurface and the scarcity of data which prevents researchers from being certain about the geology of a region in which there is limited subsurface data (Kelkar & Perez, 2002).

In cases where geological structures are continuous enough throughout the reservoir, even if minor inconsistencies exist in some locations within the field, it is assumed to be appropriate that the reservoir can be modeled as a whole using variogram-based modeling (Nobre & Sykes, 1992). Kriging is a widely used, conventional estimation technique based on a linear estimation procedure expected to provide accurate predictions of values within a volume, over an area, or at an individual point within a specified field (Kaur & Rishi, 2018). In earth science, kriging is a favored interpolation approach compared to other methods because of its ability to include the anisotropy that rock layers of a sedimentary material exhibit in geological formations. Thus, models that are obtained via the use of kriging have more resemblance to the true field geology (PetroWiki, 2020). This is in part because the linear-weighted averaging methods used in kriging techniques depend on direction as well as orientation, instead of only depending on distance as other interpolation methods do. Kriging is explained by the following expression:

$$Z^*\left(\vec{x}_p\right)=\sum_{i=1}^{n}\lambda_i Z\left(\vec{x}_i\right)$$

where $Z^*(\vec{x_i})$ = value at a neighboring location , $(\vec{x_i})$, λ_i = weight of neighboring value and $Z^*(\vec{x_p})$ = estimated value at the unsampled location (Uyan & Dursun, 2021). The estimation procedure calculates the weights λ_i (assigned to neighboring locations, which depend on the spatial relationship between unsampled points and neighboring values as well as the spatial relationship between neighboring points (Uyan & Dursun, 2021). The relationships are obtained via the use of a variogram model.

Ordinary kriging is by far the most used kriging approach that allows for the local mean to vary and be re-estimated based on nearby (local) values, thereby easing the assumption of first-order stationarity (Satish Kumar & Rathnam, 2020). Ordinary kriging is better suited for this type of analysis because a true stationary global mean value for data in a reservoir is typically unknown. It cannot be assumed that the sample mean is the same as the global mean because in any real reservoir the local mean within a neighborhood in the field can easily vary over the spatial domain (Kelkar & Perez, 2002).

Another approach to characterize reservoirs is the use of conditional simulation techniques. One of the distinguishing factors of simulation methods is that the variance observed in the data is preserved by relaxing some of the constraints of kriging, as opposed to only preserving the mean value as is done in interpolation (Kim et al., 2020). Conditional simulation is a type of variation of conventional kriging, but it is a stochastic modeling approach that allows for the calculation of multiple equally probable solutions (i.e., realizations) of a regionalized variable by simulating the various attributes at unsampled locations instead of estimating them (PetroWiki, 2016). A 'conditional' simulation is conditioned to prior data, or in other words, the raw data measurements and their spatial relationships such as a variogram are honored (Kelkar & Perez, 2002). This approach helps represent the true local variability by providing several alternate equiprobable realizations, thereby helping to characterize local uncertainty (Caers & Zhang, 2004). This is one of the most useful properties of a conditional simulation because all models are subject to uncertainty, in particular, geological models because they are based on partial sampling. This is especially true for a reservoir model due to the several different sources of uncertainty (Kelkar & Perez, 2002).

Provided that the true value of an attribute is a single number, but that exact value is always unknown, the practice in statistical modeling is to transform the single number into a random variable, a variate, which is a function that specifies its probability of being the true value for every likely outcome (Kelkar & Perez, 2002) (Kim et al., 2020) (Caers & Zhang, 2004). During each individual run the corresponding realization starts with a unique random 'navigational path' through the discretized volume providing the order of cells (or points) to be simulated (Kim et al., 2020). Because the 'path' differs from each realization-to-realization, the results provide differences throughout the unsampled cells which yield the local changes in the distribution of rock properties throughout the reservoir that are of interest for accurate geological representations. Running several realizations produces several values per variate, allowing for a graphical representation of the results and an approximation of the variates (Olea et al., 2012). It is assumed that the geologic facies vary smoothly enough across the reservoir (typical depositional setting of shallow marine reservoirs), as opposed to sharp changes in the shape of the sedimentary body.

Sequential simulation methods are some of the most widely used in practice where unsampled locations are sequentially and randomly simulated until all points are included (Elfadil et al., 2018). The order and the way that locations are simulated determine the nature of the realizations. Sequential Gaussian Simulation (SGS) is one of the most popular techniques, it assumes the data follow a Gaussian distribution (Kim et al., 2020). Because SGS is best suited for simulating continuous petrophysical variables it is deemed most appropriate for this study.

Both ordinary kriging and SGS are well proven approaches to characterizing a reservoir. A useful approach is to use both and compare and contrast the results. When including the simulation approach, the natural variability of the local geology counters the blunt smoothing effects of kriging (Kim et al., 2020). The novelty of this study is the combination of conventional kriging and conditional simulation of borehole data points for sandstone model evaluation. The goal of this investigation is to create a model to be utilized for reservoir engineering and help the development of the oilfield by identifying the best target areas to drill and perform oil recovery practices.

Study Area and Geology

Study Area

This project evaluates the Michelin sandstone reservoir within the Abacherli lease of the Mahala oil field in the eastern edge of the Los Angeles Basin of Southern California, situated within the Chino Hills along the Chino fault (Figure 1). The reservoir surface area consists of hills dissected by deep canyons with elevation changes from approximately 500 feet (152 meters) to 1,200 feet (366 meters) above sea level. The Chino Hills were formed by uplift of the two regional geologic faults, Whittier and Chino. The sedimentary basin of Los Angeles consists primarily of coastal lowlands and Upper cretaceous-cenozoic rocks in the surrounding hills (Madden & Yeats, 2008) (Figure 2).

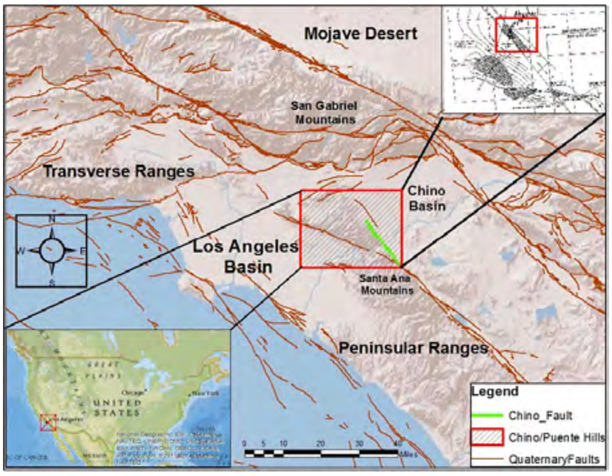

Figure 1. Location map of the study area region

Geology

Compressional forces from the Chino fault resulted in deformation creating the Mahala anticline structure (Madden & Yeats, 2008) (Figure 3). The structure is an asymmetric northwest-trending breached anticline extending over 3 miles (4.83 kilometers) in length (Dorsey, 1993). The anticline is thrust-faulted by the chino fault, which trends to the northwest and has a dip range between 50-70° to the southwest (Olson, 1977). The Chino fault thrust sliced and segmented the northeastern-most limb of the Mahala anticline fold dividing the area into a hanging wall above the fault and a footwall below the fault (Madden & Yeats, 2008) (Figure 4). This local mechanism is responsible for formation of the updip fault trap for the oil accumulation of the Michelin reservoir. The reservoir itself is a tilted homocline with steeply but uniformly dipping beds to the northeast with an approximate strike of 315°. The reservoir dip angle ranges between 40-70° with an average of 60°, and the dip angle is largest closer to the fault and decreases with distance from the fault. Two northeast-southwest trending sealing faults seal the reservoir at its northern and southern edges (Figure 5).

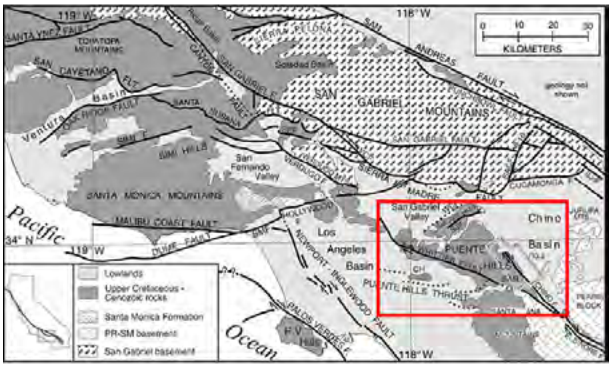

Figure 2. Geological overview of the Los Angeles Basin (Madden & Yeats, 2008)

The depositional environment is marine to moderately deep marine with sediment being deposited via the transport mechanisms of the sea and rivers, and with major subsidence and deposition occurring between the Upper Miocene until the Lower Pleistocene epochs (Yerkes et al., 1971). The strata range from Late

Cretaceous to Holocene, with the oldest Cretaceous section underlain by a basement rock of Mesozoic age consisting of granodiorite and associated plutonic rocks of the Southern California batholith from a depth of 5,000 feet (1,524 meters) to 7,000 feet (2,134 meters) (Olson, 1977). Following the law of superposition, it is expected that the layering order of the sedimentary rocks will follow the sequence on the stratigraphic column. However, the movement of the thrust fault has reversed the normal order by pushing up rocks of a lower layer over rocks of a higher layer, so older strata southwest of the Chino fault, such as the Yorba shale member thrust over younger Sycamore Canyon sand member to the northeast. At present, the overthrust hanging wall block above the fault contains the lower permeability shaly member, and the footwall block, including the Michelin reservoir, contains the higher permeability oil-rich sand (Olson, 1977). The "Michelin Zone" reservoir is predominantly a sandstone facies with some interbedded thin layers of silty and shaly sands underlain by poorly consolidated basal conglomerates (Dorsey, 1993). Observations of the lithology include tan to brown sand with a fine to coarse grain size, white to light gray and dark gray ultrafine grain size shale and siltstone, and pebble to cobble size, hard, poorly consolidated conglomerates in a calcareous matrix (Dorsey, 1993). The production sands are estimated to have an average permeability of around 500md and a porosity of 27% (Dorsey, 1993). The available isopach map (Figure 5) helps illustrate the stratigraphic thickness of the formation and reservoir boundaries.

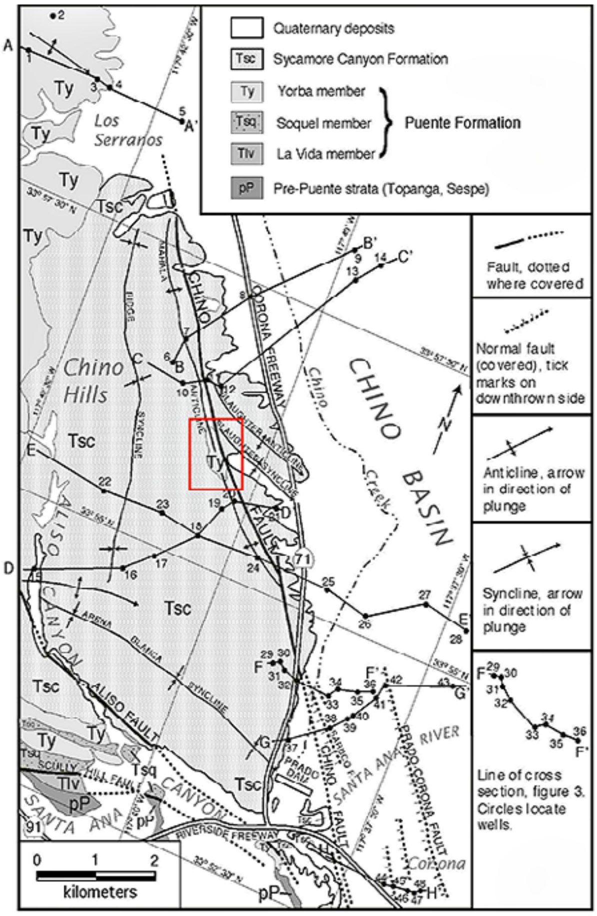

Figure 3. Geological map of the Chino Hills (Madden & Yeats, 2008)

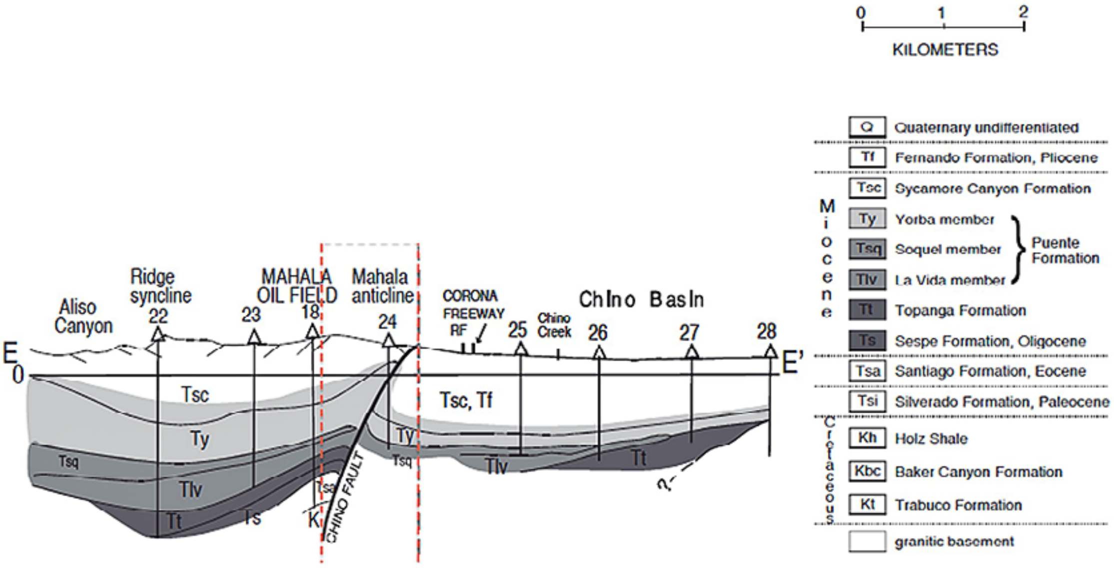

Figure 4. Cross-section of Chino fault study area for line E-E' of Figure 3 (Madden & Yeats, 2008)

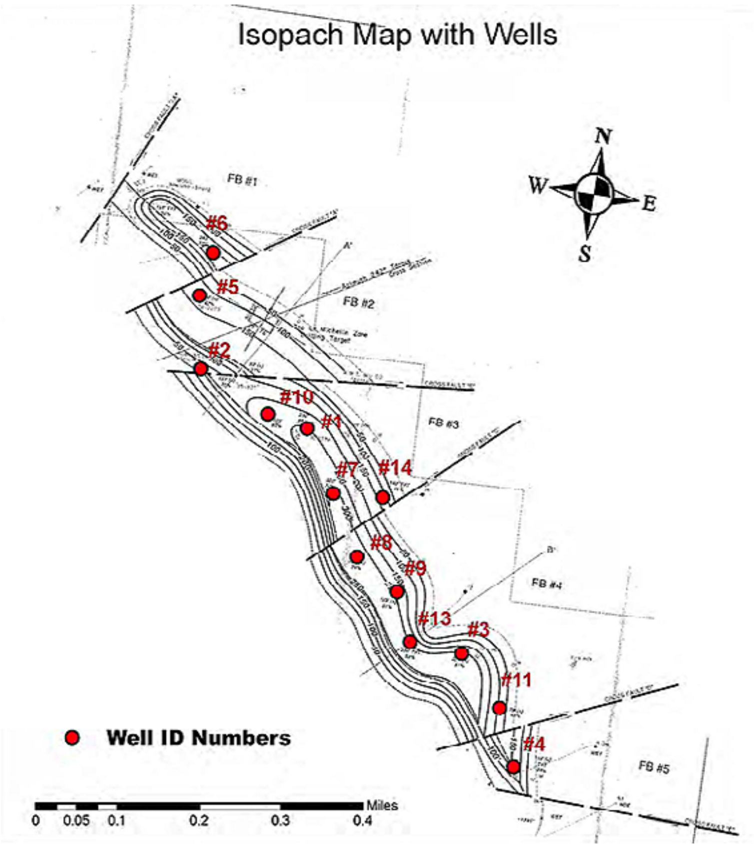

Figure 5. Isopach map of the Michelin Zone reservoir with drilled wells (Dorsey, 1993)

Data and Methods

Data

The data consisted of electrical logs for thirteen wells given as resistivity values (“R”) measured in ohms (Ω) and spontaneous potential values (“SP”) measured in millivolts (mv). The electrical logs used in this study were performed by Schlumberger Limited and the wireline services produced a continuous dataset for each of the boreholes with intervals of 10 feet (3 meters).

A 3D cross-section of the lithological boundaries inferred from the log data. (Figure 6).

An ultra-high-resolution point data set was generated based on the available isopach map. Due to the very large size of the point data set (>1.5 million

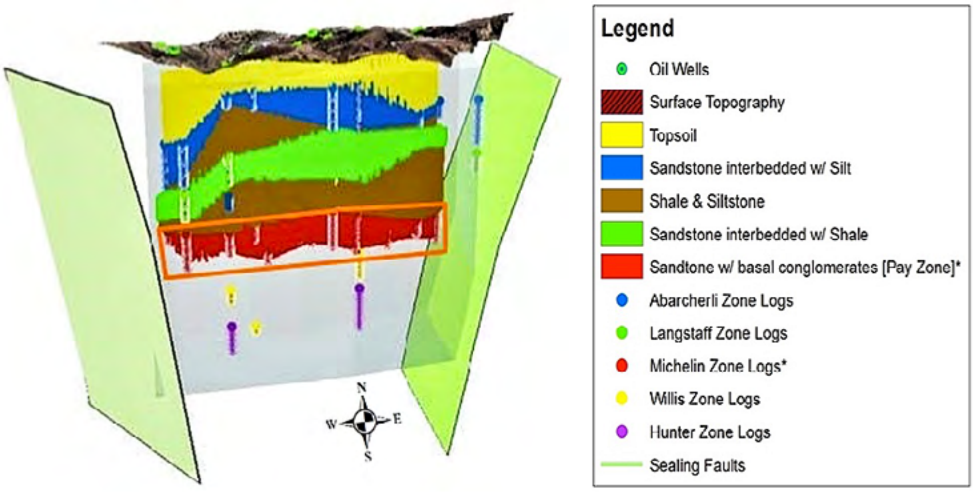

Figure 6. 3D Well Log Stratigraphic Digitization Model. Orange box depicts study area reservoir illustrating the boundaries for all interpolated and simulated models (seen in Figures 8-13)

points) running all simulations was computationally demanding, taking a total time of over one month for completing 101 realizations using a Dell XPS-8300 desktop with a Windows 7 professional 64-bits operating system.

Methods

Since ordinary kriging and conditional simulation methods are modeled by a Gaussian process, univariate and bivariate statistical tests were performed to determine if the data required transformation. The data values were inputted into the geostatistics modeling software (Figure 7 (a-b)), and a Probability Density Function (PDF), Cumulative Distribution Function (CDF), QQ-plot and a scatter plot were constructed. Colorbars indicate range of SP and R values.

The PDF and CDF outputs of the raw SP dataset followed an acceptable normal distribution. Therefore, further transformation for this dataset was not deemed necessary. The PDF and CDF of the raw R dataset displayed a significant positive skew to the right and thus were not normally distributed. It was therefore necessary to transform this dataset to normality. The R dataset was transformed to a normal distribution by using a histogram transformation tool.

The Q-Q plot of both the SP and original R probabilities plotting their quantiles against each other compares the shapes of the two probability distributions and allows to better determine if the data is close to a normal distribution. For the compared probability distributions to be normal, the plotted points should lie within a straight line. The closer all points are to a straight line, the closer the samples are to a normal distribution. The original graph illustrates that there is a significant offset, indicating a clear deviation from normality. The Q-Q plot of the SP dataset with the normally transformed R dataset illustrates a linear relationship between the two variables where the points plot across a straighter line indicating a more normal distribution.

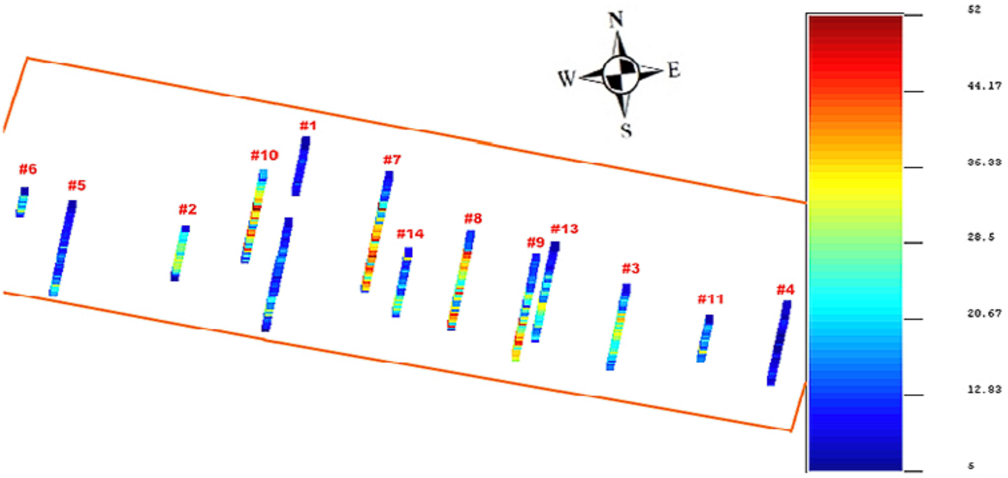

Figure 7a. R Well Data Logs with well ID numbers within study area boundary

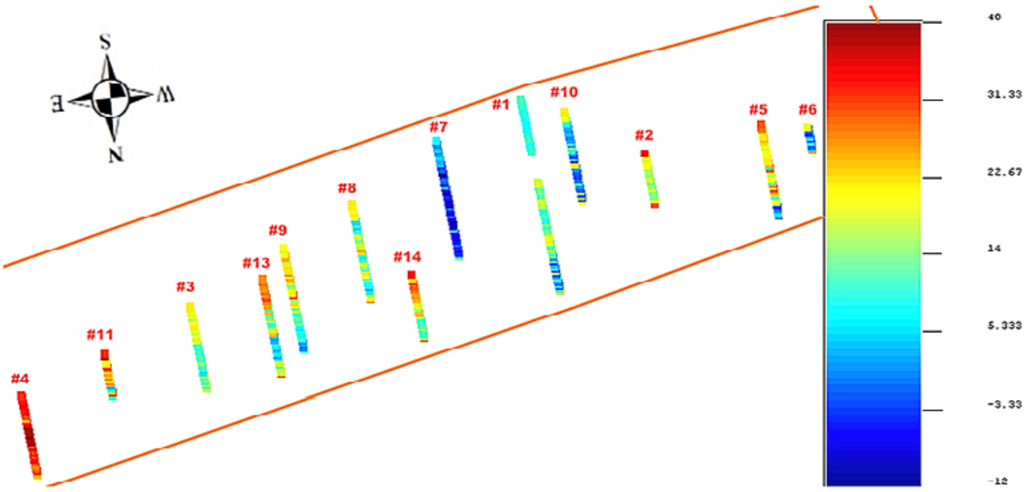

Figure 7b. SP Well Data Logs with well ID numbers within study area boundary

To establish the variogram parameters, the data was first input into the modeling software and the lag components that define the distance and the directional components that define the direction/orientation were selected. The three lag distance components are: 1) number of lags, 2) lag separation and 3) lag tolerance and the four lag direction components are: 1) azimuth, 2) dip, 3) tolerance and 4) bandwidth.

A useful technique to help estimate the parameters is to restrict the maximum distance at which the variogram is computed while retaining enough data points for a reliable estimate for that given distance. A common approach to select that restricted distance is to use half of the maximum possible distance within the region of stationarity and use it as the lag distance (Kelkar & Perez, 2002). Because a variogram is symmetric, this approach still ensures that all pairs on either side of a given location are included in the model. In addition, another common approach is to use approximately half the distance of the lag separation as the lag tolerance (Babish, 2000). These lag assumptions are not necessarily applicable to every case, since the conditions (geologic structure, well geometry, depositional settings) of different reservoirs may require significantly different lag parameters. However, since the wells in this field are oriented in nearly a straight axis, the well spacing is consistently distributed at closely uniform intervals, and the total area of the field is of modest size, this entire reservoir system is treated as a whole, and these factors and assumptions are applied in the variogram analysis.

Lag distance is equal to the number of lags times the lag separation. The maximum distance between any two well data points is 4,300 feet (1,311 meters), therefore the maximum lag distance the model was initially targeted to have was around 2,150 (655). After several attempts with the given directions, a lag number of 39 and a lag separation of 55 provided promising preliminary variogram plots. A lag tolerance half the value of the lag separation was targeted, so the value selected was 27 (55 ÷ 2= 27.5)) rounded down to the nearest whole.

Four components define the directionality of the variogram: azimuth, dip, tolerance, and bandwidth. The azimuth and dip, analogous to geologic strike and dip, are two important components reflecting the major axes in a 3D environment, and the tolerance and bandwidth help further refine the directions of interest to accommodate the intended directionality of the field. By adjusting the variogram azimuth, dip, tolerance, and bandwidth, it is possible to capture the structural geology of the field (strike, dip, rake, plunge) and hence end up with a true volumetric estimation that resembles the geological structure. A general direction was first established by selecting the azimuth and dip, and then the tolerance and bandwidth were adjusted until a variogram structure was identified. Three variogram directions were established: a vertical direction, an omni-directional and a major direction in the horizontal axis which followed the geological strike of the reservoir.

The first direction established was the vertical direction with an azimuth of zero, a dip of 90°, a tolerance of 5° and a bandwidth of 200. The second direction established was omnidirectional with an azimuth of 0°, a dip of 0°, a tolerance of 91°, and a bandwidth of 200. The third direction established was the horizontal direction aligned along the strike of the reservoir with an azimuth of 120°, a dip of 10°, a tolerance of 40°, and a bandwidth of 500. The interpreted variogram structure for each dataset in each direction was fitted with the best fit function. After several attempts adjusting the variogram design for both datasets in terms of the specific modeling components and variogram parameters, a final best-fit variogram model was established for each dataset.

As part of the interpolation, the variance was also mapped, identifying the areas with higher or weaker variance. Cross-validation of the results involved leaving one data location out and performing the estimation to predict the value at that excluded location, repeating the process by removing one different well location at a time, then re-running the estimation until all the well values have been interpolated. Once the predicted values were obtained for the data at all the well locations, they were compared to the known values to help determine the accuracy of the model.

The uncertainty throughout the field was characterized by examining the differences among the multiple equiprobable realizations, which display the local variations. In this matter, if uncertainty at a particular location is relatively small, then a number of images should display similar simulated values at that location. Conversely, if uncertainty at a particular location is relatively large, then a majority of images should display the differences in simulated values at that location.

Since the primary objective of performing a stochastic simulation is to create a model for the probability distribution of the unknown variables and because the variables are conditioned to the data, which is assumed to be a true representation of the subsurface geology, then their values are reasonably expected to fall within the limits of the simulated probability distribution. Summary statistics performed on the simulation output provide a measure of the uncertainty of the model, and specific statistical calculations on the suite of realizations provided estimated probabilities. Calculating the median of the resulting multivariate distribution from all the realizations yielded a map with the highest probability of representing the true model. This probability model was compared to the predicted (kriged) model, and the similarity provided a degree of confidence. In addition to the median probability (i.e., P50), the P10 and P90 quantiles provided uncertainty ranges in the simulated median value, and thus more confidence that the true expected mean value falls within the simulated range.

Results

The correlation coefficient between R and SP was -0.665. This strong negative correlation follows the trend expected in a petroleum field since large positive R spikes and large negative SP deflections are clear indicators of permeable hydrocarbon-containing formations.

A total of 53 realizations of SP distribution across the field using Sequential Gaussian Simulation (SGS) were generated. Six randomly selected SP SGS realizations are illustrated (Figure 8).

A total of 48 realizations for R distribution across the field using SGS were generated. Six randomly selected R SGS realizations are illustrated (Figure 9).

The calculated median (P50), as well as the P10 and P90 maps for R were generated (Figure 10). Higher R values shown in red in Figure 10 are scattered, but a cluster is apparent in center area of reservoir.

The calculated median (P50) as well as the P10 and P90 maps for SP were generated (Figure 11). Higher

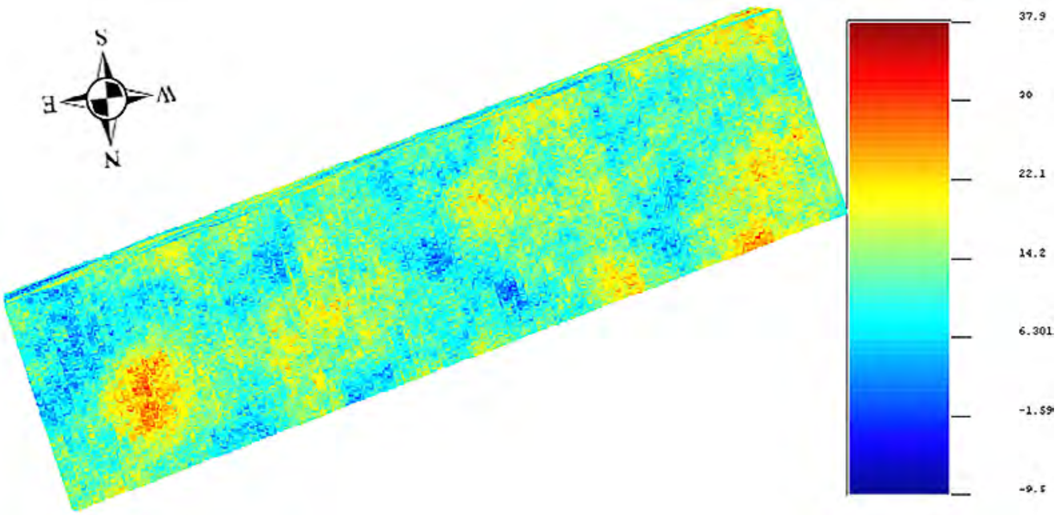

Figure 8a. SP Realization Example #1

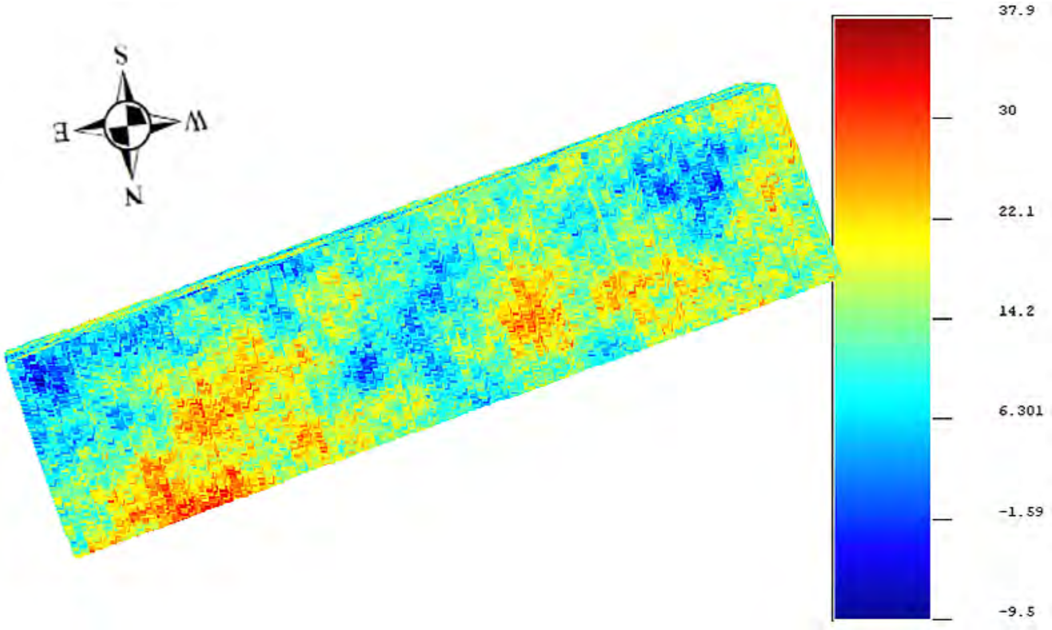

Figure 8b. SP Realization Example #2

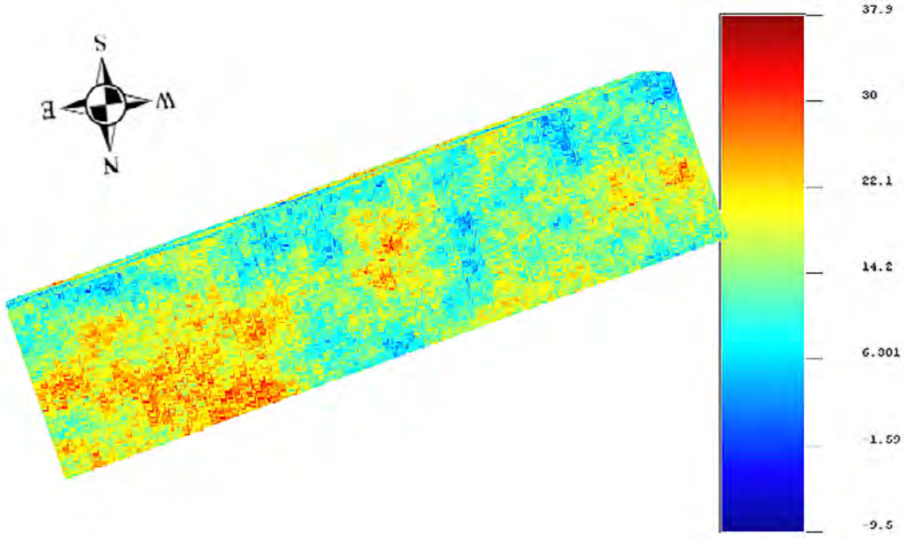

Figure 8c. SP Realization Example #3

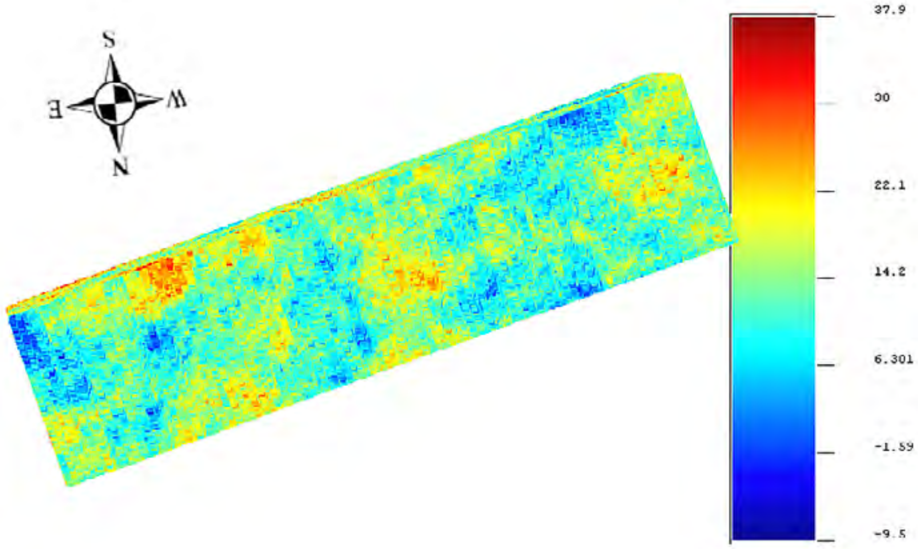

Figure 8d. SP Realization Example #4

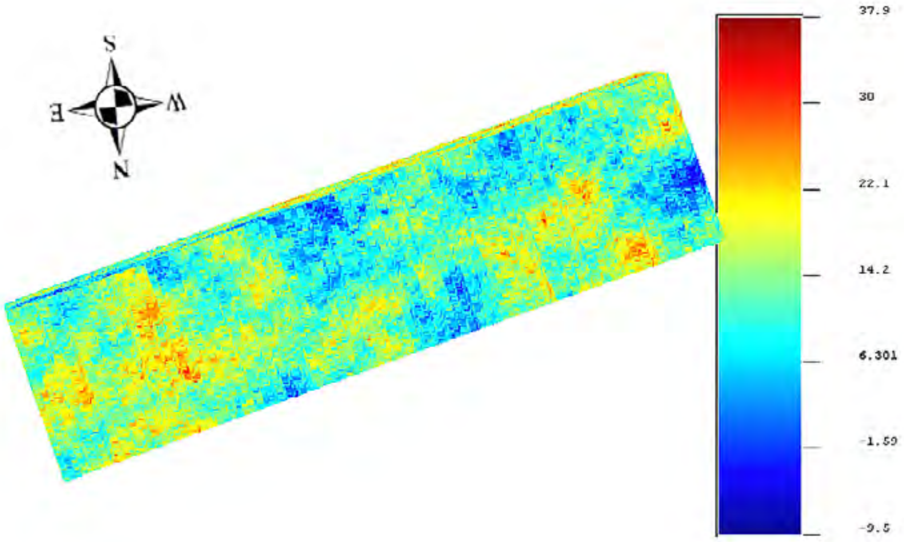

Figure 8e. SP Realization Example #5

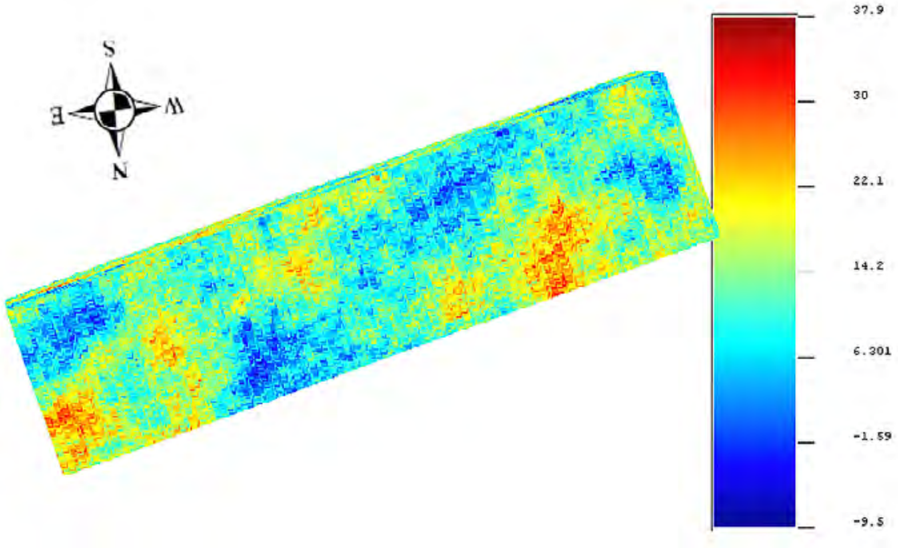

Figure 8f. SP Realization Example #6

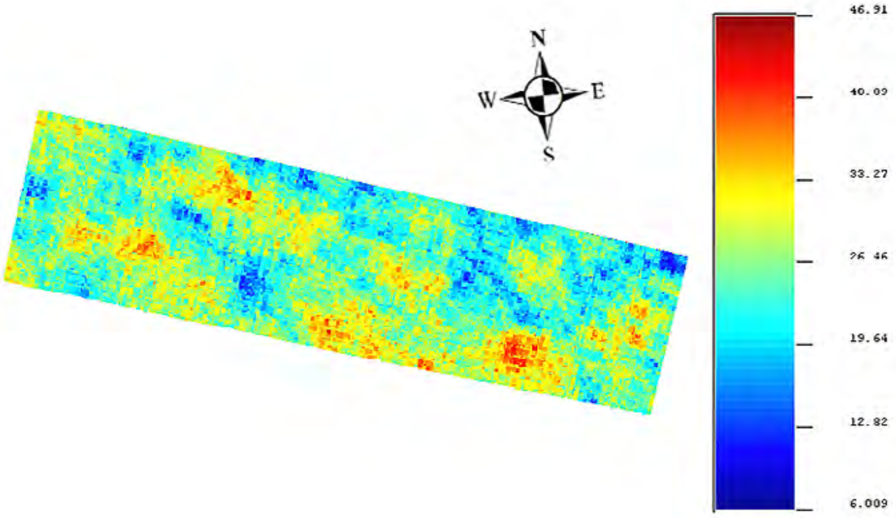

Figure 9a. R Realization Example #1

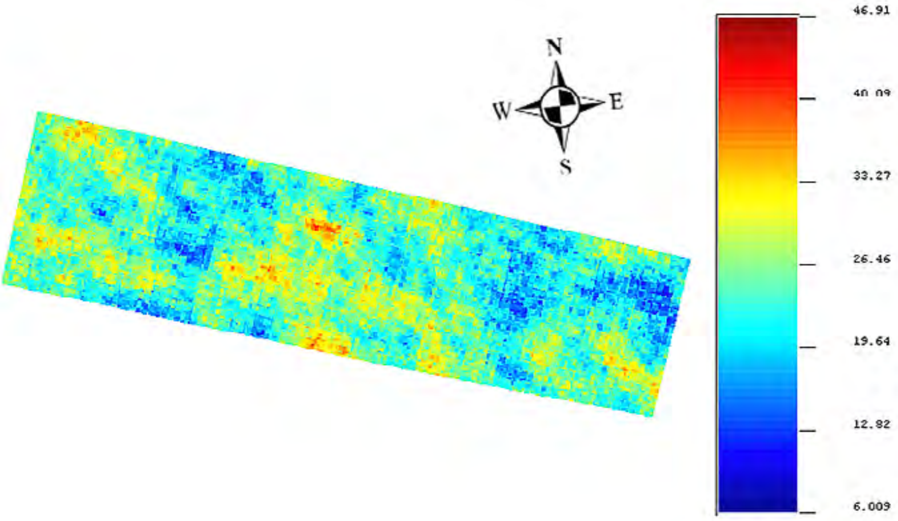

Figure 9b. R Realization Example #2

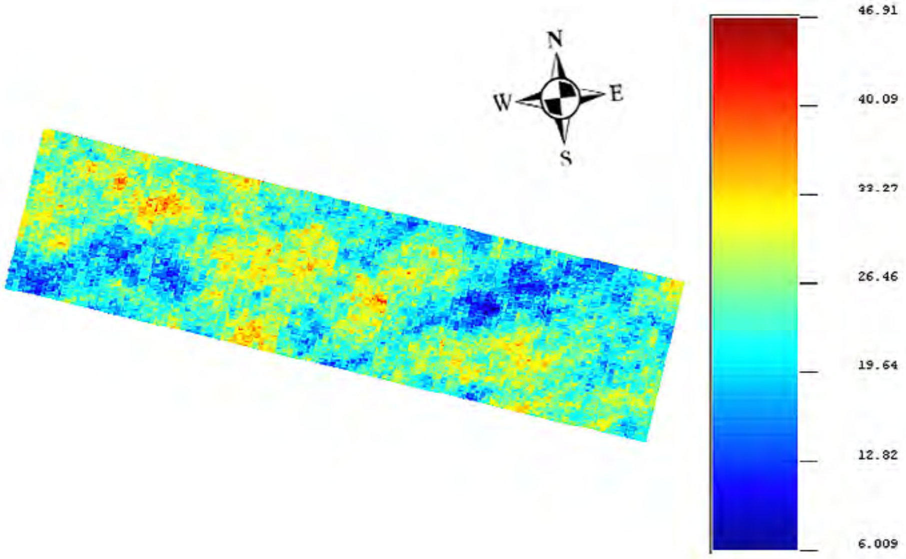

Figure 9c. R Realization Example #3

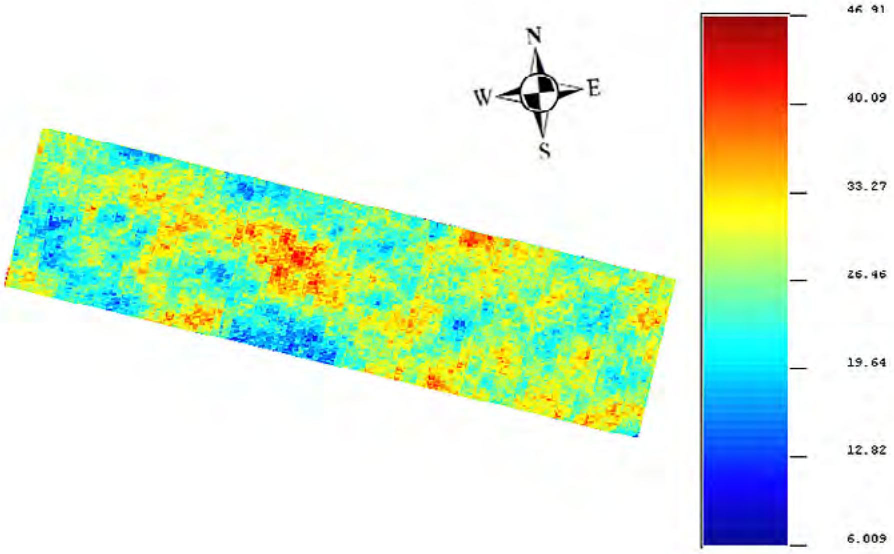

Figure 9d. R Realization Example #4

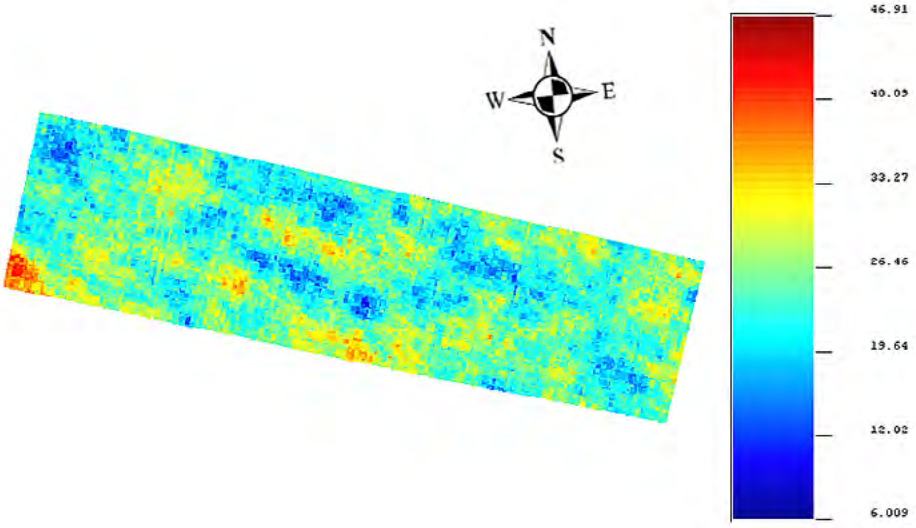

Figure 9e. R Realization Example #5

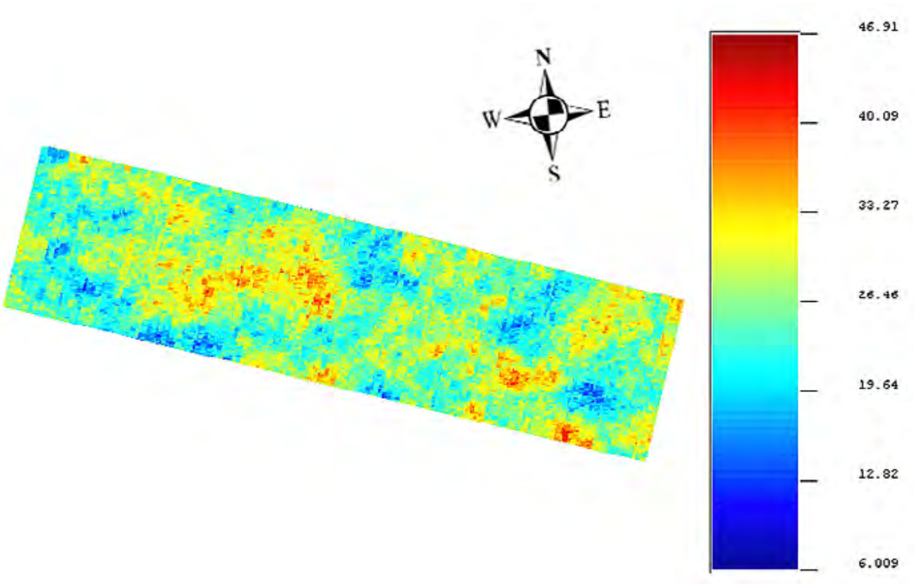

Figure 9f. R Realization Example #6

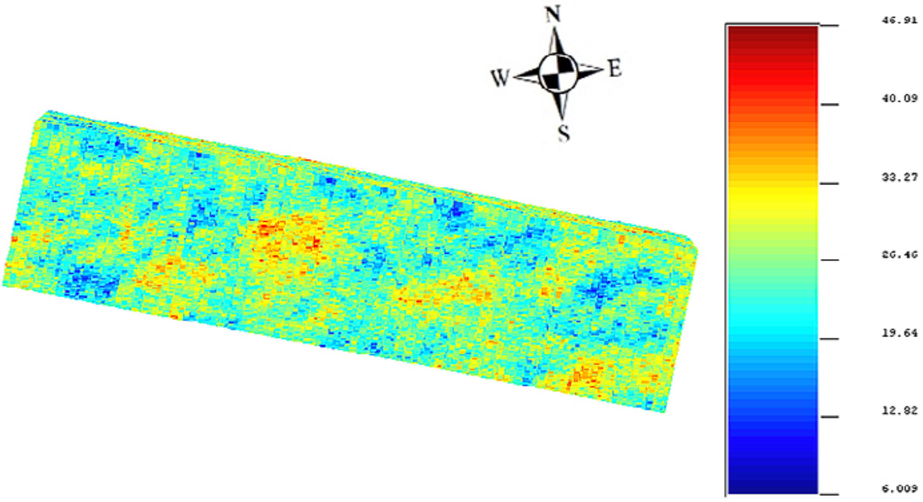

Figure 10a. R P50 model

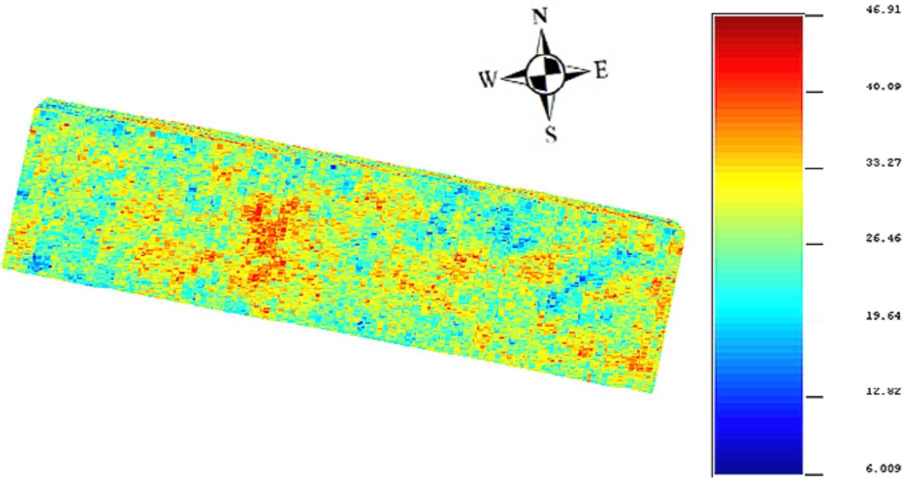

Figure 10b. R P10 model

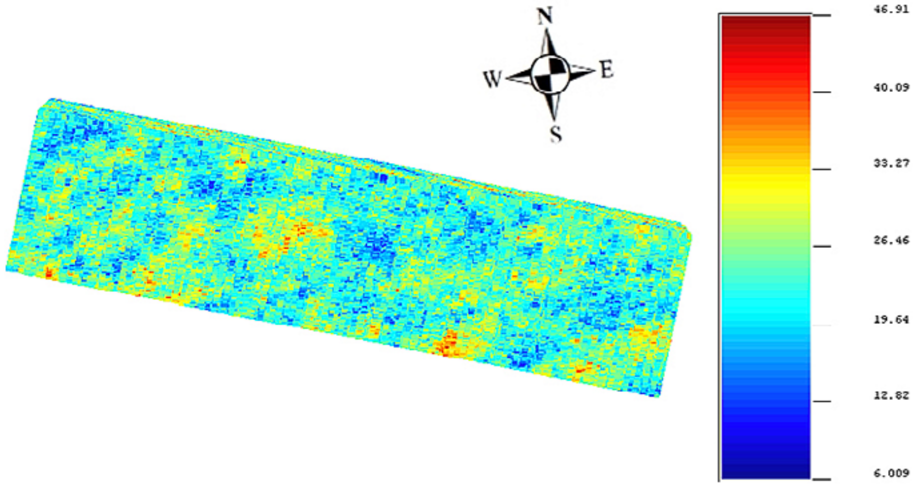

Figure 10c. R P90 model

red SP values are evident in the southeastern area of the reservoir, while scattered, lower blue SP values are apparent in the center area as well as near the top of the southeastern area, especially in the P50 and P90 models.

The models were interpolated, and their derived variance maps were generated for both R and SP datasets (Figures 12 and Figure 13).

In Figure 12, higher R values in red are evident in the middle of the reservoir, and decrease outward from the middle to the edges of the reservoir, and the variance is less in middle and gradually increases (with darker shades) towards the corners.

Lower SP values indicated in blue are centered in the middle, top section of the reservoir, and gradually decrease toward opposite edges. Higher SP values in red are concentrated in the southeastern section of the reservoir. The variance is low in the southeastern section and towards the center of the reservoir, while it increases in the top corners (Figure 13).

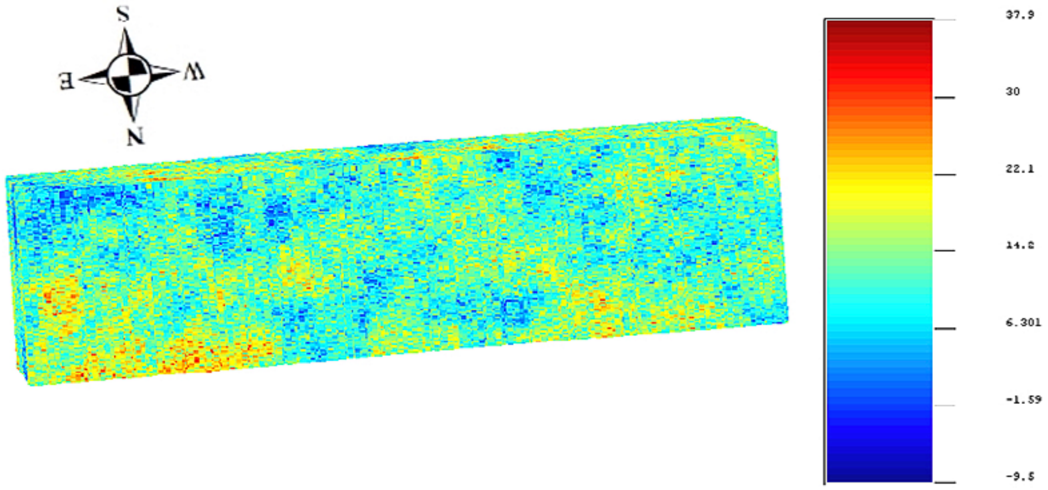

Figure 11a. SP P50 model

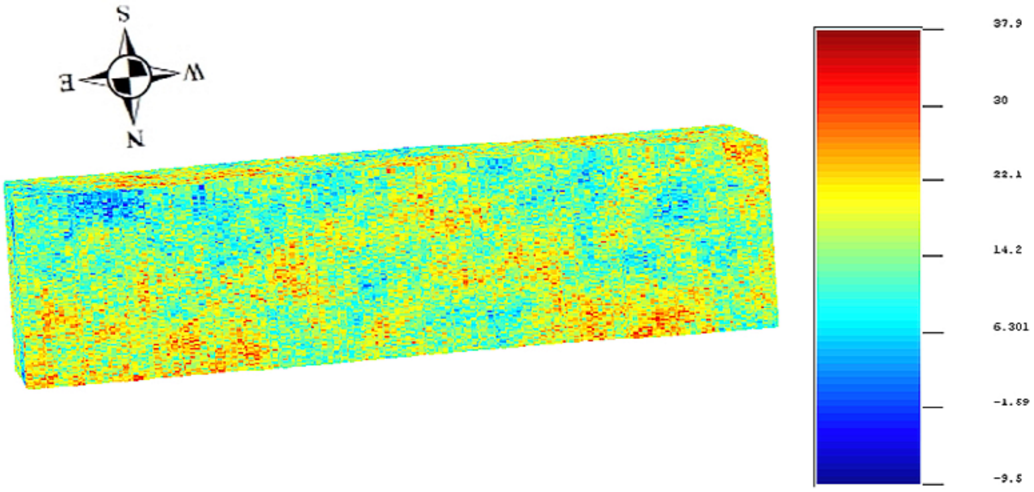

Figure 11b. SP P10 model

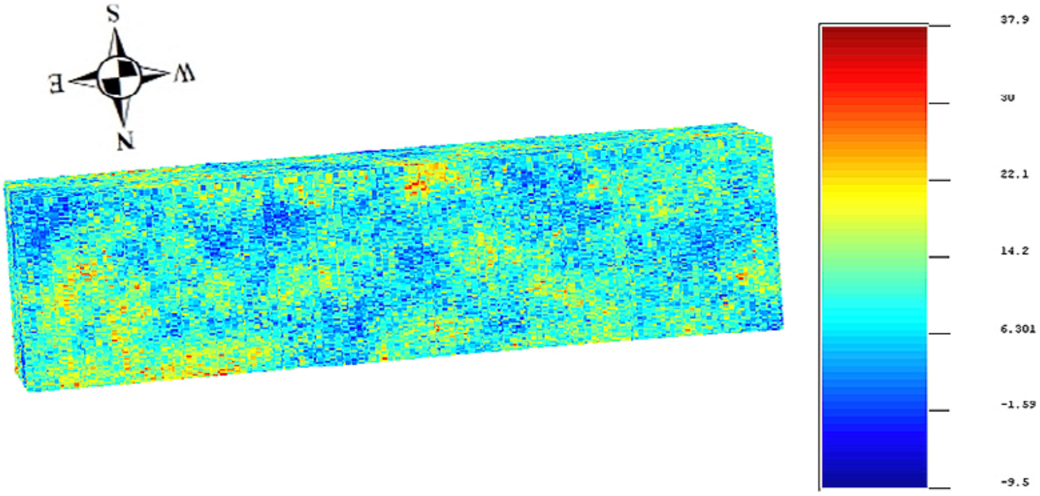

Figure 11c. SP P90 model

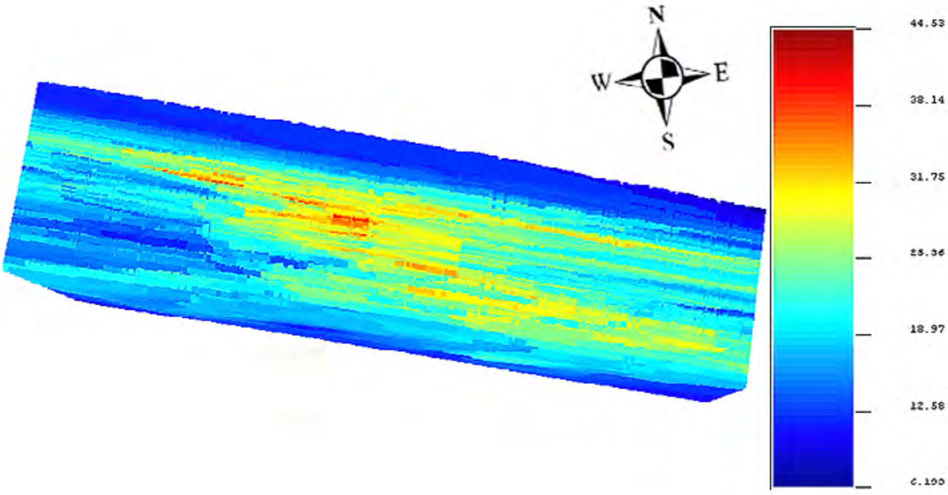

Figure 12a. R kriging map

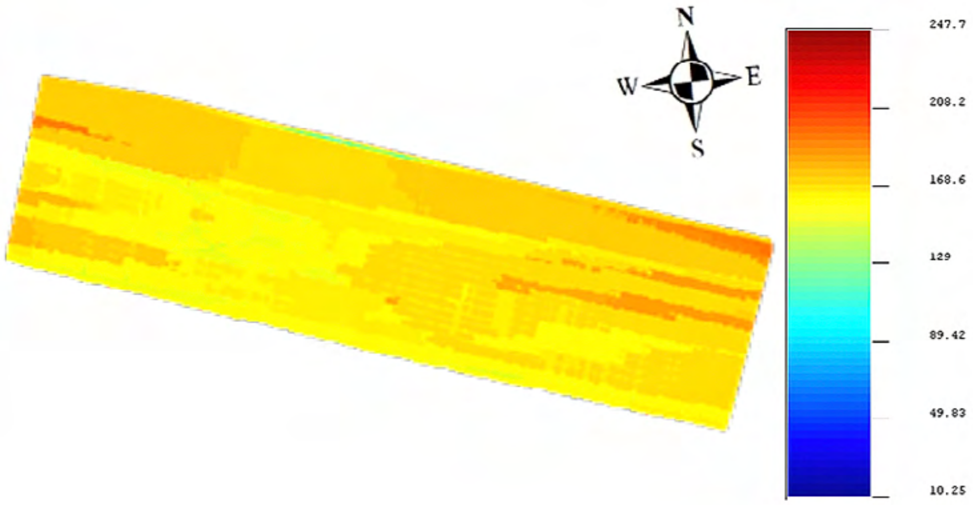

Figure 12b. R variance map

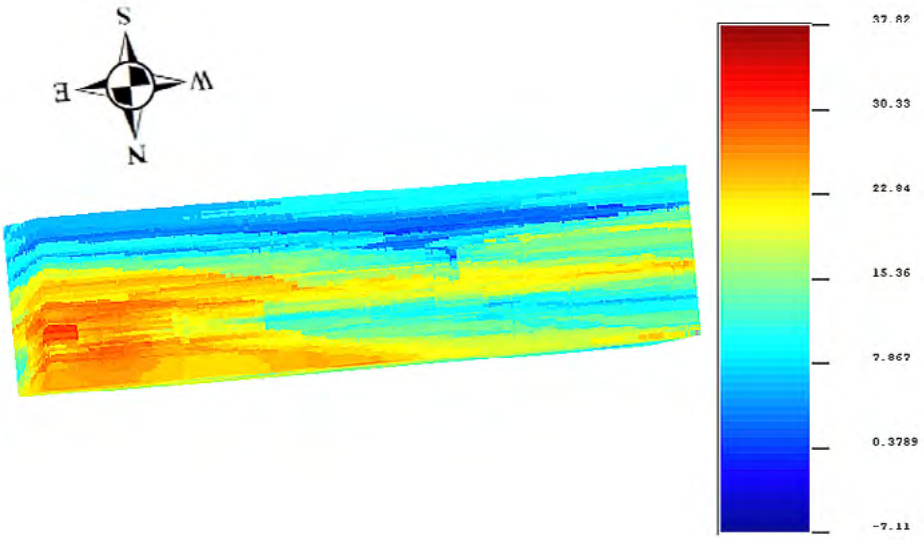

Figure 13a. SP kriging map

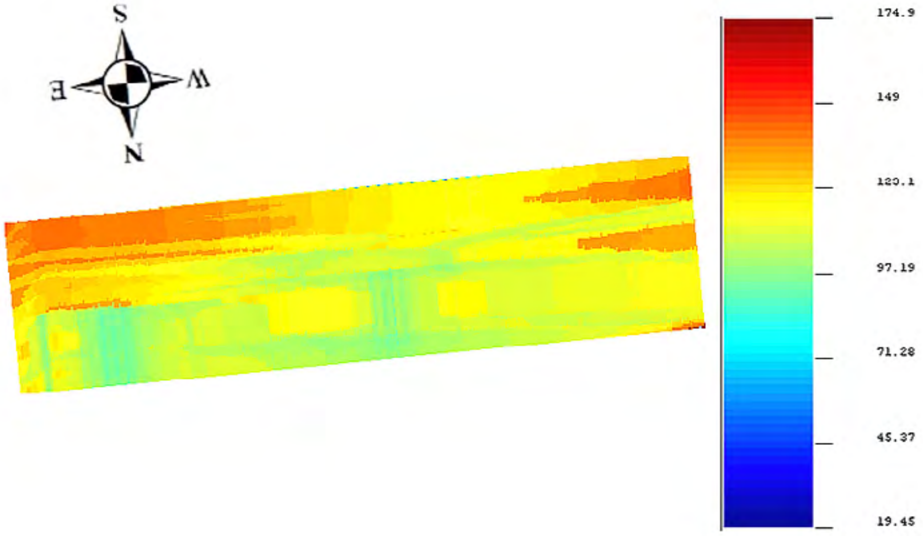

Figure 13b. SP variance map

Discussion

The vertical variograms for both datasets exhibit periodic behavior, which represents cyclical sedimentary processes. This is known as the "hole effect" and is typically experienced when modeling variograms in the vertical direction. In depositional environments, sediment is deposited in layers during geological events, thus this repetition of cycles will be reflected in the vertical continuity of the layers in the field. In these variograms, the transition from one stratum to another can be clearly defined. Interpretation from both vertical variograms indicates that the formation is continuous up to around 350 feet (107 meters) and then becomes discontinuous but regains continuity at greater distances. This trend is expected to continue throughout different depths across the reservoir. The fitted vertical variogram functions only include those values up to 350 feet because it is useful to only capture the extent of the continuous data. In addition, the average thickness of the producing formation is only 378 feet (115 meters), so most of the vertical extent is included by modeling to 350 feet. The fitted functions of the other two directional variograms were plotted to include as many of the data points as possible. A few local outliers were excluded in order to obtain a reasonable structural variogram model. Overall, the trend of the field appears to be well captured in the variogram models.

Since all the realizations honor the same constraints because they are coming from the same distribution, it is not possible that one realization is more likely to occur than any other. Therefore, the apparent differences between realized images are representative of the local uncertainty and visualizing their variability provides a reasonable assessment of uncertainty. Provided the distribution is representative of the real field then the true reservoir values are expected to fall within the bounds of the distribution while the calculated statistical summaries of the simulation (P10, P50, P90) illustrate the probabilities of occurrence.

The cross-validation included the observed data plotted with the estimated data versus subsea depth. All the plots include low, medium, and high-value thresholds as well as horizontal error bars of the standard deviation of the observed data.

Comparing the kriged R model with the simulated R P50 model, it appears that the overall trend generally remains consistent between both models except for a few small patches in the upper half of the field. Comparing the kriged SP model with the simulated SP P50 model, it appears that most of the continuity is also well preserved, especially in the lower half of the field. However, small to moderate dissimilarity appears within the upper half of the field. The dissimilarities that are most apparent occur mainly near opposite edges, which is probably due to the lack of data from boreholes drilled near the edges. Greater uncertainty is expected near the corners because the edges are further away from the observed values. The P10 and P90 maps appear to show a modest margin of probability in the distribution in which the P50 median falls between the lower and upper quantiles. The noticeable differences apparent in both datasets in the upper half of the models are probably related to more significant geological variability in the upper half of the reservoir.

Standard deviation error bars help provide a "tolerance range" in the cross-validation to better gauge interpolation accuracy. Well#1 had the largest error in the R dataset, followed by the southernmost well#4. Although these wells plot in a consistent manner close to the observed values, most of the calculated values fall outside the bounds of the standard deviation. The estimated values for the rest of the wells in this dataset appear to plot reasonably close to the observed values. Close examination of the R results revealed that the estimations for all the wells between well#1 and well #4 (i.e. in the lower half of the field) appear to plot slightly better than all of the wells north of well #1 (i.e. in the upper half of the field).

Well#7 had the largest error in the SP dataset, plotting outside the bounds of the standard deviation. Most of the other wells within this dataset also plot reasonably close to the observed values. Nevertheless, some significant differences were noted, including well #4 (located at the southern edge) and well #6 (located at the northern edge) which both show significant deviation. The "dataset outlier" for SP is well #7 and for R values is well #1. The same field observation is noted in both the R and SP results, where all the wells in the lower half (south of their respective "dataset outlier") provide slightly closer approximations relative to all the wells in the upper half (north of the dataset outlier).

The relatively larger margin of error of the two wells at the edges can be attributed to their more isolated locations compared to the other wells. The clustered borehole locations have more conditioning data and so are expected to provide slightly more accurate estimates. Given a general consistency between the kriged and simulated models, in addition to the same general trend expressed from the cross-validation of both datasets. It can be assumed that the southern half of the field, from well #4 up to somewhere between well #7 and well#1, is very continuous and the upper half, from well #1 to well#6, is slightly less continuous. The results of this study indicate that the reservoir is intact with a well-defined continuity trend mimicking the geologic attitude of the field. As can be seen from similarities between the northwest-southeast direction and the omni-direction variograms, the continuity in the study area is preferential in the plane parallel to the geological strike. Because all the wells are preferentially directed along this plane, there is inherently more certainty in the data obtained in this direction (northwest-southeast) compared to the perpendicular direction (southwest-northeast). Furthermore, because of the continuous thrust faulting that extends the reservoir along the strike and thins the geologic units along the perpendicular plane, it is expected that the trend along the plane perpendicular to the strike will be less continuous. Similarly, because a coherent continuity trend is captured in the vertical direction, the uncertainty in this direction is minimal.

Other similar studies have been conducted on oilfield reservoirs, yet with notable differences compared with the study described herein. For example, Gringarten and Deutsch, 1999 describe proper use of variogram modeling but do not illustrate conditional simulation evaluations. Sabouhi et al. (2019) conducted variogram-based modeling of a hydrocarbon field using sequential indicator simulation rather than sequential gaussian simulation. Masaud and Meddaugh, 2019 conducted reservoir characterization via geostatistical modeling but due to facies heterogeneity, use of a pillar gridding technique to establish a structural framework, and use of a conceptual facies model were warranted.

Conclusion

A geologic model was created using a two-point geostatistics approach that characterizes the distribution of electrochemical properties. The study area represents a conventional sandstone oil reservoir. Evaluation of the data obtained from electrical logs warranted ordinary kriging and sequential Gaussian simulation as appropriate methods for the analyses. A best fit variogram function incorporating geological and statistical assumptions was defined and used for the analyses. Results included 3D models and multiple equiprobable realizations of the geological continuity of SP and R. With respect to associated uncertainties, the confidence level in the models is preferential relative to the direction where it is strongest vertically, then parallel to the geologic strike, and then perpendicular to strike. Validation procedures included cross-validation and calculating the P10, P50, and P90 quantiles to assess local uncertainty and variability. By comparison and evaluation, it can be concluded that the results provided a practical reservoir model. Although the structural continuity of the reservoir appears to retain general consistency throughout the field, there is an apparent continuity trend where the northern half of the reservoir becomes slightly less continuous relative to the southern half. It is assumed that this small to modest change reflected from the field continuity is due to geological phenomena attributed to the localized thrusting of the Chino fault.

References

Babish, G. (2000). *Geostatistics Without Tears: A Practical Guide to Geostatistics, Variograms and Kriging*. Regina, Sask: Environment Canada, Ecological Research Division, Environmental Conservation Branch.

Caers, J., & Zhang, T. (2004). *Multiple-Point Geostatistics: A Quantitative Vehicle for Integrating Geologic Analogs into Multiple Reservoir Models*. Stanford, Calif: American Association of Petroleum Geologists. https://doi.org/10.1306/M80924C18

Caumon, G., (2010). Towards Stochastic Time-Varying Geological Modeling. *Mathematical Geosciences*, 42(5), 555-569. https://doi.org/10.1007/s11004-010-9280-y

Deutsch, C.V. (2006). What in the reservoir is geostatistics good for? *Journal of Canadian Petroleum Technology*, 45(4). https://doi.org/10.2118/06-04-DAS

Dorsey, R. (1993). *Geologic Review Abacherli Lease Mahala Field: Eastern Puente Hills San Bernardino, California*. KMT Oil Company

Dubrule, O., & Damsleth, E. (2001). Achievements and Challenges in Petroleum Geostatistics. *Petroleum Geoscience*, 7(S), S1-S7. http://dx.doi.org/10.1144/petgeo.7.S.S1

Ebong, E., Akpan, A., Ekwok, S., Esu, E., & Ebong, L. (2021). 3-D reservoir characterization and hydrocarbon volumetric estimation of parts of Niger Delta Basin-Nigeria. *Journal of African Earth Sciences*, 180, 104207. https://doi.org/10.1016/j.jafrearsci.2021.104207

Elfadil, M., Al-Yaqout, A., & Hefny, A. (2018). Volumetric soil profile modeling using geo-statistics and GIS: case study Kuwait Sabkha. *Arabian Journal of Geosciences*, 11(7). https://doi.org/10.1007/s12517-018-3474-x

Gorell, S. (1995). Using geostatistics to aid in reservoir characterization. *The Leading Edge*, 14(9), 967-974. http://dx.doi.org/10.1190/1.1437188

Gringarten, E., & Deutsch, C.V. (1999). *Methodology for Variogram Interpretation and Modeling for Improved Reservoir Characterization.* Society of Petroleum Engineers Annual Technical Conference and Exhibition. Houston, Texas. https://doi.org/10.2118/56654-MS

Journel, A.G. (2000). Geostatistics and Petroleum Geology. *Mathematical Geology*, 32(1), 139-141. https://doi.org/10.1023/A:1007563003567

Kaur, L. & Rishi, M., (2018). Integrated geospatial, geostatistical, and remote-sensing approach to estimate groundwater level in North-western India. *Environmental Earth Sciences*, 77(23). https://doi.org/10.1007/s12665-018-7971-8

Kelkar, M., & Perez, G., (2002). *Applied geostatistics for reservoir characterization.* Richardson, Tex: Society of Petroleum Engineers.

Kim, M., Kim, H., & Chung, C., (2020). A Three-Dimensional Geotechnical Spatial Modeling Method for Borehole Dataset Using Optimization of Geostatistical Approaches. *KSCE Journal of Civil Engineering*, 24(3), 778-793. https://doi.org/10.1007/s12205-020-1379-1

Madden, C., & Yeats R. (2008). *Paleoseismic and Structural Investigations to Determine Late Quaternary Slip Rate for the Chino Fault, Southeastern Los Angeles Basin, California.* United States Geological Survey: 04HQGR0107

Masaud, M., & Meddaugh, W.S. (2019). Reservoir Characterization-Geostatistical Modeling of the Paleocene Zelten Carbonate Reservoir. Case Study: Meghil Field, Sirte Basin, Lybia. *Society of Petroleum Engineers Annual Technical Conference and Exhibition*. Calgary, Alberta. https://doi.org/10.2118/195988-MS

Nobre, M., & Sykes, J., (1992). Application of Bayesian Kriging to subsurface characterization. *Canadian Geotechnical Journal,* 29(4), 589-598. https://doi.org/10.1139/t92-066

Olea, R., Charpentier, R., Cook, T., Houseknecht, D., & Garrity, C. (2012). Geostatistical Population-Mixture Approach to Unconventional-Resource Assessment with an Application to the Woodford Gas Shale, Arkoma Basin, Eastern Oklahoma. *SPE Reservoir Evaluation & Engineering,* 15(05), 554-562. https://doi.org/10.2118/163049-PA

Olson, L. (1977). *Mahala oil field and vicinity.* Sacramento: California Division of Oil & Gas.: TR18.

PetroWiki (2016). *Geostatistical conditional simulation - PetroWiki.* [online] Available at: <https://petrowiki.spe.org/Geostatistical_conditional_simulation> [Accessed 20 July 2021].

PetroWiki (2020). *Kriging and cokriging - PetroWiki.* [online] Available at: <https://petrowiki.spe.org/Kriging_and_cokriging> [Accessed 20 July 2021].

Sabouhi, M., Azad, M.N., & Rezaee, P. (2019). Geostatistical Lithofacies Modeling of Carbonate-Evaporite Succession-Kangan Formation-Based on Variography Analysis and Sequential Indicator Simulation Method in One of the Hydrocarbon Fields of Persian Gulf. *Petroleum Research*, 29(108), 42-45. DOI: 10.22078/pr.2019.3630.2655

SatishKumar, K., & Rathnam, E.V. (2020). Regional Optimization of Existing Groundwater Network Using Geostatistical Technique. *Numerical Optimization in Engineering and Sciences,* 979, 93-106.

Uyan, M., & Dursun, A. (2021). Determination and modeling of lignite reserve using geostatistical analysis and GIS. *Arabian Journal of Geosciences*, 14(4). https://doi.org/10.1007/s12517-021-06633-2

Yerkes, R., McCulloh, T., Schoellhamer, J., & Vedder, J. (1971). *Geology of the Los Angeles Basin, California-an Introduction.* Washington: U.S. G.P.O.: 420-A